

# Biased liquid crystal infiltrated photonic bandgap fiber

**Weirich, Johannes; Lægsgaard, Jesper; Scolari, Lara; Wei, Lei; Alkeskjold, Thomas Tanggaard; Bjarklev, Anders Overgaard**

*Published in:*
Optics Express

*Link to article, DOI:*
10.1364/OE.17.004442

*Publication date:*
2009

*Document Version*
Publisher's PDF, also known as Version of record

# Biased liquid crystal infiltrated photonic bandgap fiber

**Johannes Weirich[1], Jesper Lægsgaard[1], Lara Scolari[1], Lei Wei[1], Thomas Tanggaard Alkeskjold[2] and Anders Bjarklev[1]**

[1]*DTU Fotonik, Department of Photonics Engineering, Technical University of Denmark Building 345v, DK-2800 Kgs. Lyngby, Denmark*

[2] *Crystal Fibre A/S, Blokken 84, 3460 Birkerød Denmark*

*jwei@fotonik.dtu.dk*

**Abstract:** A simulation scheme for the transmission spectrum of a photonic crystal fiber infiltrated with a nematic liquid crystal and subject to an external bias is presented. The alignment of the biased liquid crystal is simulated using the finite element method to solve the relevant system of coupled partial differential equations. From the liquid crystal alignment the full tensorial dielectric permittivity in the capillaries is derived. The transmission spectrum for the photonic crystal fiber is obtained by solving the generalized eigenvalue problem deriving from Maxwell's equations using a vector element based finite element method. We demonstrate results for a splay aligned liquid crystal infiltrated into the capillaries of a four-ring photonic crystal fiber and compare them to corresponding experiments.



**OCIS codes:** (060.2310) Fiber optics; (230.3720) Liquid-crystal devices

## References and links

1. P. St. J. Russell, "Photonic crystal fibers, " Science **299**, 358-362, (2003)
2. A. Bjarklev, J. Broeng, and A. S. Bjarklev, "Photonic Crystal Fibres" (Kluwer Academic, Dordrecht, 2003)
3. C. Kerbage, R. S. Windeler, B. J. Eggleton, P. Mach, M. Dolinski, and J. A. Rogers, "Tunable devices based on dynamic positioning of micro-fluids in micro-structured optical fiber," Opt. Commun. **204**, 179–184 (2002)
4. T. T. Larsen, A. Bjarklev, D. S. Hermann and J. Broeng, "Optic devices based on liquid crystal photonic bandgap fibres," Opt. Express **11,** 2589–2596 (2003)
5. T. T. Alkeskjold, J. Lægsgaard, A. Bjarklev, D. S. Hermann, A. Anawati, J. Broeng, J. Li, and S. Wu, "All-optical modulation in dye-doped nematic liquid crystal photonic bandgap fibers," Opt. Express **12,** 5857–5871 (2004)
6. M. W. Haakestad, T. T. Alkeskjold, M. D. Nielsen, L. Scolari, J. Riishede, H. E. Engan and A. Bjarklev, "Electrically tunable photonic bandgap guidance in a liquid crystal filled photonic crystal fiber," IEEE Photon. Technol. Lett. **17**, 819-821, (2005)
7. L. Scolari, T. T. Alkeskjold, J. Riishede, A. Bjarklev, D. Hermann, A. Anawati, M. Nielsen, P. Bassi, "Continuously tunable devices based on electrical control of dual-frequency liquid crystal filled photonic bandgap fibers," Opt. Express **13** , 7483-7496 (2005)
8. T. R. Wolinski, K. Szaniawska, S. Ertman, P. Lesiak, A. W. Domanski, R. Dabrowski, E. Nowinowski-Kruszelnicki and J. Wojcik, "Influence of temperature and electrical fields on propagation properties of photonic liquid-crystal fibres," Meas. Sci. Technol. **17**, 985-991 (2006)
9. L. Scolari, T. T. Alkeskjold, A. O. Bjarklev, "Tunable gaussian filter based on tapered liquid crystal photonic bandgap fibre," Electron. Lett. **42**, 1270-1271, (2006)
10. D. Nordegraaf, L. Scolari, J. Lgsgaard, L. Rindorf, and T. T. Alkeskjold, "Electrically and mechanically induced long period gratings in liquid crystal photonic bandgap fibers," Opt. Express **15**, 7901–7912 (2007)
11. T. T. Alkeskjold, L. Scolari, D. Noordegraaf, J. Laegsgaard, J. Weirich, L. Wei, G. Tartarini, P. Bassi, S. Gauza, S. T. Wu, A. O. Bjarklev, "Integrating liquid crystal based optical devices in photonic crystal fibers," Opt. Quantum Electron. **39** , 1009-1019, (2007)
12. P. D. de Gennes, "The Physics of Liquid Crystals," (Clarendon,1974)

#105241 - $15.00 USD Received 12 Dec 2008; revised 31 Jan 2009; accepted 3 Mar 2009; published 5 Mar 2009

13. J. Lægsgaard, "Modelling of a biased liquid-crystal capillary waveguide," JOSA B **23**, 1843–1851 (2006)
14. S. V. Burylov, "Equilibrium configuration of a nematic liquid crystal confined to a cylindrical cavity," J. Exp. Theor. Phys. **85**, 873–886 (1997)
15. J. Li and S. T. Wu, "Extended Cauchy equations for the refractive indices of liquid crystals,", J. Appl. Phys. **95**, 896–901 (2004).
16. N. M. Litchinitser, S. C. Dunn, P. E. Steinvurzel, B. J. Eggleton, T. P. White, R. C. McPhedran, C. M. de Sterke, "Application of an ARROW model for designing tunable photonic devices," Opt. Express **12**, 5857–5871 (2004)

## 1. Introduction

During the last years, Liquid Crystal (LC) infiltrated Photonic Crystal Fibers (PCFs) [1],[2] have attracted high interest due to their unique optical properties giving the possibility to use them as a basis technology for optical components.

By infiltrating micro structured fibers with suitable materials, tunability is achieved [3]. Due to their birefringence, dielectric anisotropy and complex alignment structure, LCs are particularly interesting materials. Infiltrating them into the capillaries of a solid core PCF changes the guiding principle from modified Total Internal Reflection (m-TIR) to bandgap guiding. Due to the physical properties of the LC, the optical characteristics of the LC infiltrated PCF and the transmission spectrum can be tuned thermally [4], optically [5] and electrically [6]-[8]. Various devices have been demonstrated, among others Gaussian filters [9] and notch filters [10], tunable polarimeters and waveplates [11] as well as rotatable and switchable polarization controllers [11].

The optical mode structure in the fiber is closely linked to the mode structure in the individual LC infiltrated capillaries and changing the orientation of the LCs in the capillaries has therefore a strong influence on the transmission spectrum. By applying an external electric field, the LC director structure reorients depending on the applied voltage, the physical parameters of the LC and the position of the capillaries in the fiber. It is important to gain an understanding of the LC alignment and the effect on the optical properties of the LC infiltrated PCF, to explain the shape of the transmission spectrum and to characterize LCs according to their physical parameters. This will be very useful for the design of new LCPCF devices. Since the complexity of the problem makes analytical approaches difficult or even impossible, simulations are employed to understand the behavior of LCPCFs under the influence of an external field. In this paper, we present a numerical scheme to simulate the change of the transmission spectrum when applying an external electric field.

In a first step we simulate the orientation of the LCs in the capillaries subject to an external bias using Finite Element Method (FEM) simulations. The orientation of the birefringent LCs is transformed into a refractive index structure for all capillaries in the fiber and used in vector element based FEM mode simulations. With this the core mode of the biased LC infiltrated fiber is obtained and the coupling loss with respect to a PCF without LC is calculated. The simulated transmission spectra for an LC infiltrated PCF with four rings of capillaries and an applied external bias of 0V, 100V and 150V are shown, and the results are compared to the experiment.

The article is organized as follows. In section 2 we describe our model for the LC alignment and present the simulation result with and without applied bias. From the LC alignment the dielectric structure of the LCPCF is obtained and we show that it varies for different capillaries in the same ring. In section 3 we use the results of the previous section to simulate the transmission spectrum for different applied bias. The results are compared to experimental data and reasons for the deviations are discussed. Section 4 summarizes and gives an outlook on further development.

#105241 - $15.00 USD Received 12 Dec 2008; revised 31 Jan 2009; accepted 3 Mar 2009; published 5 Mar 2009

## 2. Modelling a biased liquid crystal infiltrated photonic crystal fibre

The local orientation of a nematic LC can in general be represented by a director vector $\hat{\mathbf{n}}(x,y,z)$. It is a unit vector pointing into the direction of the rod axis of the LC (see inset Fig. 1), giving information about the LC's local electric, optical and mechanic properties. We simulate the orientation of the director vector under an applied external bias, for all capillaries of a PCF. A schematic illustration of the configuration is shown in Fig. 1.

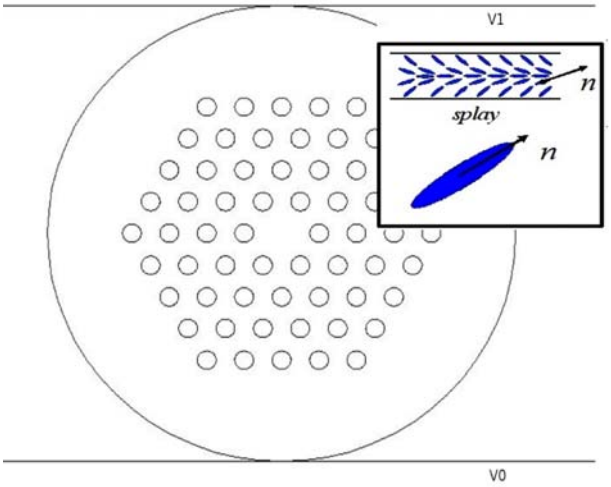


Fig. 1. Schematic illustration of the photonic crystal fiber with four rings of LC infiltrated capillaries and placed between two electrodes. The fiber is surrounded by air. Inset: The director vector for a splay aligned LC

The PCF we consider has four rings of capillaries and is placed between two electrodes which are on a potential V1 and V0 respectively. The fiber is surrounded by air and the capillaries are infiltrated with a nematic LC. We model the alignment of the director when applying an external bias. The Partial Differential Equations (PDEs) describing the orientation of the director vector follow from minimizing the LC's free energy [12] subject to some boundary conditions. We consider only two contributions, the elastic free energy and the electric free energy, which are

$$F[\mathbf{n}] = F_0 + F_{el} = \int_\Omega d\Omega \left( \frac{k_1}{2}(\nabla \cdot \mathbf{n})^2 + \frac{k_2}{2}(\mathbf{n} \cdot \nabla \times \mathbf{n})^2 + \frac{k_3}{2}(\mathbf{n} \times \nabla \times \mathbf{n})^2 \right) - \int_\Omega d\Omega \left( \frac{1}{2}\mathbf{D} \cdot \mathbf{E} \right) \tag{1}$$

Here, $k_1, k_2$ and $k_3$ are the elastic constants of the LC. $k_1$ describes the energy contribution to the LC's free energy from director configurations with non-vanishing divergence (splay-alignment), $k_2$ describes twisted and $k_3$ bended structures. The last term in Eq. 1 is the electric free energy, with $\mathbf{D} = \varepsilon \mathbf{E}$. Using only these two contributions corresponds to assuming fixed boundary conditions, and is reasonable for PCFs with relatively large capillaries with respect to the rod size of the LCs [13]. A more stringent simulation would demand to add boundary terms in Eq. 1 [14]. Since the director vector is a unit vector, it has only two degrees of freedom, and we can therefore represent the components $\hat{\mathbf{n}} = (n_x, n_y, n_z)$ by introducing two angels $\theta$ and $\phi$, with $\theta$ the angle between the director and the capillary axis, which we chose to be the $z$-axis, and $\phi$ the angle between the directors in-plane components and the local radial unit vector $\hat{\mathbf{e}}_\mathbf{r}$. Figure 2 shows how the director vector in each of the individual capillaries is expressed in terms of the two angles. The center of the capillary is at the coordinates $(x_0, y_0, 0)$ and the local radial

#105241 - $15.00 USD Received 12 Dec 2008; revised 31 Jan 2009; accepted 3 Mar 2009; published 5 Mar 2009

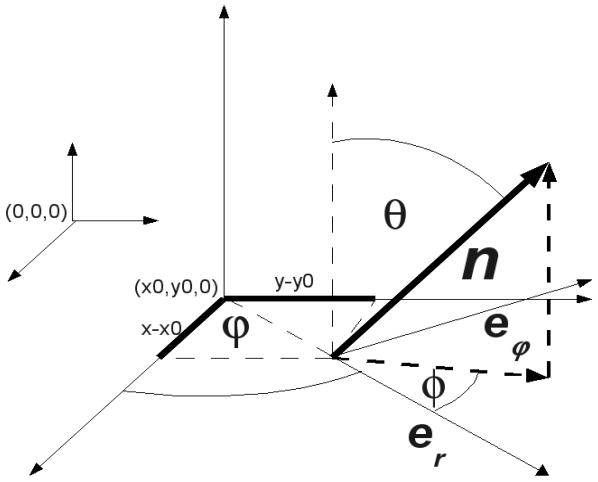


Fig. 2. Schematic illustration of the director vector expressed by the cylinder like coordinates $\theta$ and $\phi$.

and azimuthal unit vectors are defined with respect to the origin lying at this point.

$$\hat{\mathbf{e}}_\mathbf{r} = \begin{pmatrix} \cos\varphi \\ \sin\varphi \end{pmatrix} \qquad \hat{\mathbf{e}}_\varphi = \begin{pmatrix} -\sin\varphi \\ \cos\varphi \end{pmatrix} \tag{2}$$

The local azimuthal angle $\varphi$ is the angle between $\hat{\mathbf{e}}_\mathbf{r}$ and the $x$-axis and given in terms of the local coordinates as $\varphi = \tan^{-1} y_{loc}/x_{loc}$. The angle $\phi$ is the angle between the projection of $\hat{\mathbf{n}}$ on the x-y plane and the local radial unit vector, whereas $\theta$ is the one between $\hat{\mathbf{n}}$ and the $z$-axis.The director vector in global coordinates is then written as

$$\begin{pmatrix} n_x \\ n_y \\ n_z \end{pmatrix} = \begin{pmatrix} \cos\phi\sin\theta\cos\varphi - \sin\phi\sin\theta\sin\varphi \\ \cos\phi\sin\theta\sin\varphi + \sin\phi\sin\theta\cos\varphi \\ \cos\theta \end{pmatrix} \tag{3}$$

with $\varphi = \tan^{-1}(y - y_0/x - x_0)$. In Eq. 3 we introduce cylindrical alike coordinates to express the director-vector field, which depend on Cartesian coordinates as the independent variables. $\theta$ is defined globally as the angle between the director and the $z$-axis, while $\phi$ is defined locally as the angle between the director and the local radial unit vector $\hat{\mathbf{e}}_\mathbf{r}$. This allows us to assign boundary conditions in a simple way by using the local cylinder symmetry of the structure, and automatically ensures the unit length of the director vector. It is important to note that we solve for both $\theta$ and $\phi$ at global points $(x,y)$, but the value for $\phi$ is obtained with respect to the local radial unit vector. The global definition of $\hat{\mathbf{n}}$ in Eq. 3 is due to expressing the local radial and azimuthal unit vectors in global coordinates $(x,y)$. Mathematically, this can be done in a very simple way, since the coordinate transformation from global to local capillary coordinates is just a translation. We use the variational form of Eq. 1, $\delta F = 0$, to model the FEM code.

A particular attention has to be paid to the electric field in Eq. 1. A change of the director structure, due to the electric field, results in a change of the dielectric structure, which in turn yields a new electric field distribution. We therefore have to consider a coupled system of PDE's, consisting of the minimization of the free energy, and Poisson's equation

$$\nabla \cdot \mathbf{D} = -\nabla \cdot \varepsilon \nabla \Phi = 0 \tag{4}$$

#105241 - $15.00 USD Received 12 Dec 2008; revised 31 Jan 2009; accepted 3 Mar 2009; published 5 Mar 2009

with the electrostatic potential $\Phi$. The dependent variables are therefore the angles $\phi$ and $\theta$ as well as the electrostatic potential $\Phi$ . Mathematically, the coupling of the electric field to the director fields is via the dielectric permittivity, which appears in Eqs. 1 and 3 and can be written in terms of the director vector as [13]

$$\varepsilon_{ij} = \varepsilon_{\perp}\delta_{ij} + \Delta\varepsilon\, n_i n_j \qquad (i,j = 1,2,3) \tag{5}$$

with $\varepsilon_{\perp}$ the dielectric permittivity component perpendicular to the LC axis, $\Delta\varepsilon = \varepsilon_{\parallel} - \varepsilon_{\perp}$ the difference between its parallel and perpendicular component and $n_i$ the $i$-th component of the director vector.

We solve this system in an iterative approach, illustrated in Fig. 3. First, the LCs free energy

$$\begin{array}{ccc} \delta F[\hat{\mathbf{n}}] = 0 & \xrightarrow{\hat{\mathbf{n}}} & \varepsilon_{ij}(\hat{\mathbf{n}}) \\ \uparrow \mathbf{E} & & \downarrow \varepsilon \\ \mathbf{E} = -\nabla\Phi & \xleftarrow[\Phi]{} & -\nabla\varepsilon\nabla\Phi = 0 \end{array}$$

Fig. 3. The iterative solution process for the system of coupled partial differential equations

is minimized without an applied electric field and the local director vector is obtained for all the capillaries. The dielectric permittivity is calculated using Eq. 5 and used as a constant in Poisson's equation. From Poisson's equation we obtain the electric field distribution $\mathbf{E} = -\nabla\Phi$, which is used as a constant contribution in the free energy, manifesting in a non vanishing last term in Eq. 1. The free energy is then minimized again and the iterative process is continued until the change in the electric field from a previous to the next simulation is below a certain threshold. The advantage of the iterative process, compared to solving for all three dependent variables at the same time is the following. Since we solve individually for the electrostatic potential and the angles $\theta$ and $\phi$, the number of degrees of freedom for each simulation is reduced. This allows for a very fine mesh around and inside the capillaries, without exceeding memory and time limitations.

To be able to compare the simulations to experimental results, we choose to simulate the splay-aligned LC MDA-00-3969 (Merck, Germany), which shows a boundary alignment of $\theta = \pi/4, \phi = 0$ (see inset Fig. 1). These values were obtained experimentally using a technology called polarization optical microscopy (POM) [7]. We infiltrated MDA-00-3969 into a 5 $\mu m$ fused silica capillary tube, comparable to the $4.3\mu m$ of the PCF capillaries. The tube is placed between two crossed polarizers, and the illuminating light is passing through the first polarizer, then through the tube and in the end through the second polarizer. Due to the birefringence of the LC we can see a light pattern indicating that the LC is aligning in a splayed configuration with an angle at the surface of $\theta = \pi/4$ [7].

The following values for $k_1, k_2, k_3$ and $\varepsilon_{\perp}, \varepsilon_{\parallel}$ for a $1kHz$ AC electric field were measured. The

Table 1. The K-constants and dielectric constants for MDA-00-3969, measured at room temperature (22° C)

| $k_1$ | $k_2$ | $k_3$ | $\varepsilon_{\perp}$ | $\varepsilon_{\parallel}$ |
|---|---|---|---|---|
| $18[pN]$ | $10.8[pN]$ | $21.1[pN]$ | 6.88 | 9.69 |

#105241 - $15.00 USD Received 12 Dec 2008; revised 31 Jan 2009; accepted 3 Mar 2009; published 5 Mar 2009

fiber we use is a Large Modea Area LMA-13 (Crystal Fibre A/S, Denmark) with four rings of capillaries, a pitch of $8.5\mu m$ and a capillary radius of $2.15\mu m$. The dielectric permittivity of the silica-materials is $\varepsilon_r = 3.91$. While in the experiment we use an AC electric field, we simulate a DC field in order to keep RAM consumption and computational time reasonably low. The dielectric properties of the LC for an AC field at 1kHz are very close to the ones for a static electric field. The relevant AC-voltage for the comparison is then the root mean square(rms) value. We choose an electric field with $0V, 100V$ and $150V$ potential difference, leading to a rotation of the LCs in the capillaries.

The simulations are done using nodal based second order finite elements on a triangular grid with a maximal element size of 3.5% of the capillary diameter within and around the capillaries, and more coarse elements further away from the capillaries. Using symmetries, we simulate only $1/4$ of the domain, in order to reduce calculation time and RAM consumption. The meshed computational domain is shown in Fig. 4. On the left side the PCF surrounded by air with the high potential condensator plate on top, and on the right hand side the mesh for one capillary.

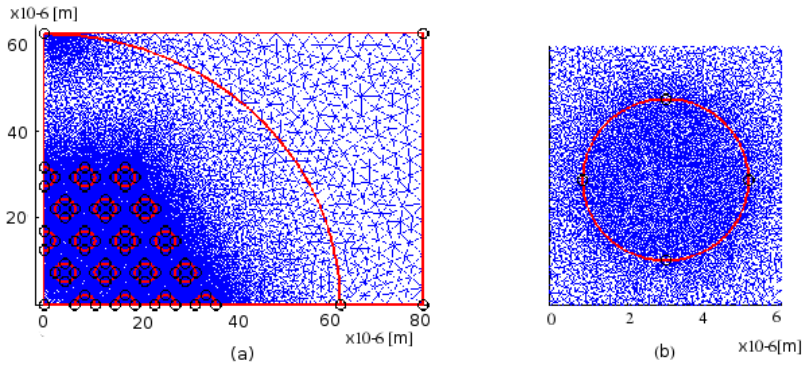


Fig. 4. The meshed computational domain. (a) The structure has been reduced to a quarter of its original size (b) the mesh for a single capillary

In Fig. 5 the absolute value of the y-component $E_y$ of the electric field is shown, and the highest values of $|E_y|$ can be found at the interface between air and Silica as shown in Fig. 5(a). To further illuminate the behavior of $|E_y|$ around the capillaries, Fig. 5(b) shows a truncated computational domain focussing on the area around the crystal structure of the PCF. Here, the $|E_y|$ values are larger for the silica area around the capillaries, while the ones inside the capillaries are lower. This is due to the higher values of the dielectric permittivity of the LC inside the capillaries, compared to the one of Silica. One also observes different values for $Ey$ inside the capillaries. This is due to the splay alignment of the LC. The electric field 'sees' both the parallel and the perpendicular component of the dielectric permittivity at the boundaries of the capillaries, while at the center it can only see the lower perpendicular component of the dielectric permittivity.

Figure 6 shows the alignment of the liquid crystal for $0V$, $100V$ and $150V$ for the capillary lying on the x-axis of the innermost ring of capillaries.

When applying a bias, the director reorients parallel to the electric field, leading to a stronger $n_y$ component, while the $n_x$ and $n_z$ components become smaller. While for 100V potential difference it is difficult to see, the variation of the director at 150V is quite obvious. In fact, Eq. 1 shows a quadratic dependence of the free energy on the electric field, and this manifests in

#105241 - $15.00 USD Received 12 Dec 2008; revised 31 Jan 2009; accepted 3 Mar 2009; published 5 Mar 2009

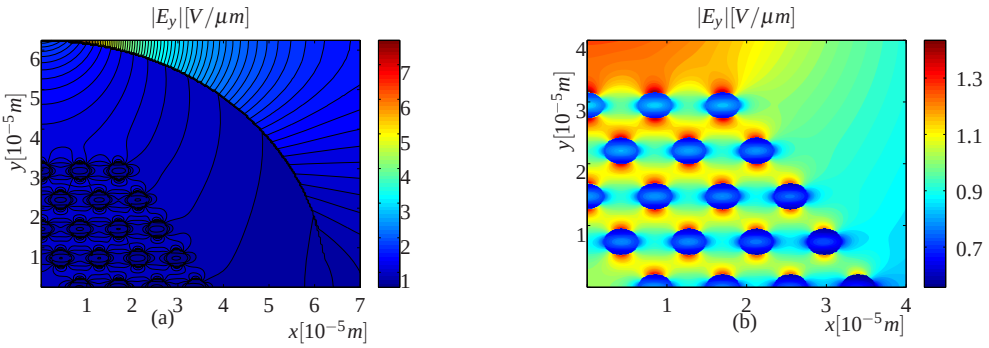


Fig. 5. Cross section plot of $|E_y|$ for an applied voltage of 150V over (a) the whole computational domain, (b) the truncated domain to illustrate the voltage drop around the capillaries

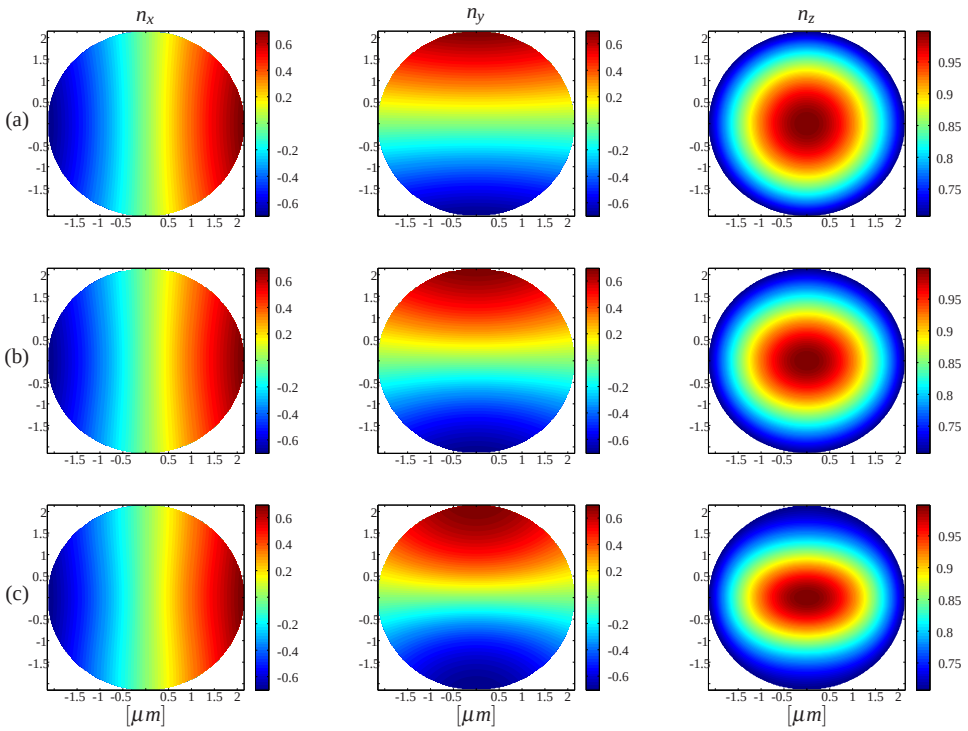


Fig. 6. The vector-components $n_x, n_y, n_z$ of the director for a) no bias, b) for 100V and c) 150V applied bias.

faster increase in the orientation change for higher voltages. To quantify the director change for different voltages, we introduce the integrated relative director change

$$\delta_{\hat{\mathbf{n}}} = \frac{\int\limits_{\Omega} d\Omega |\hat{\mathbf{n}}_{\mathbf{V}} - \hat{\mathbf{n}}_{\mathbf{0}}|}{\int\limits_{\Omega} dxdy |\hat{\mathbf{n}}_{\mathbf{0}}|} \tag{6}$$

with $\hat{\mathbf{n}}_{\mathbf{V}}$ the director for an applied bias, and $\hat{\mathbf{n}}_0$ the one without. Figure 7 shows the averaged $\delta_{\hat{\mathbf{n}}}$ values for the different rings, $< \delta_{\hat{\mathbf{n}}} >= 1/M \sum\limits_{m} \delta_{\hat{\mathbf{n}}}$, with $M$ the number of capillaries in the ring, for different applied voltages. The average director variation changes little for different rings,

#105241 - $15.00 USD Received 12 Dec 2008; revised 31 Jan 2009; accepted 3 Mar 2009; published 5 Mar 2009

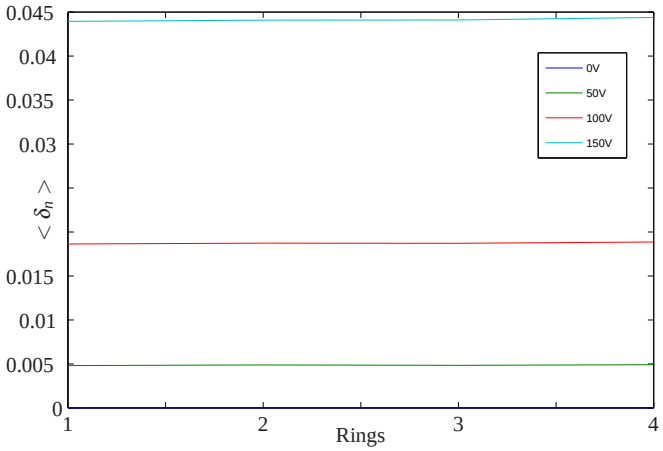


Fig. 7. Average integrated relative director change depending on the different rings of the fiber. The various curves reflect different voltages

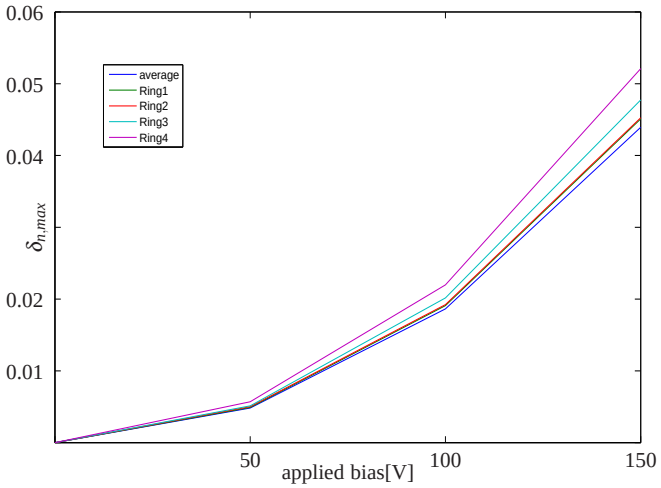


Fig. 8. Maximum $\delta_{\mathbf{n}}$ for the different capillaries compared to the average variation, taken over all capillaries

as expected from previous result for the strength of the electric field in the capillaries shown in [7]. Nevertheless, $\delta_{\hat{\mathbf{n}}}$ is very different within the same ring of capillaries. Figure 8 compares the averaged relative director change which in this case is taken over all capillaries, with the maximum director change for the different rings. The maximum variation of the outermost ring is of order 10% greater than the the average variation. This behavior, and the fact, that the alignments in different capillaries influence each other due to the coupling to the electric field, show the necessity to actually simulate the alignment in all rings of an LC infiltrated PCF, in order to obtain a reliable director structure which can be used in mode simulations.

#105241 - $15.00 USD Received 12 Dec 2008; revised 31 Jan 2009; accepted 3 Mar 2009; published 5 Mar 2009

## 3. Simulation of the bandgap shift

From the alignment of the LC in the capillaries of the PCF we obtain the dielectric structure of the optical system by replacing $\varepsilon_\perp$ and $\varepsilon_\parallel$ in Eq. 5 with their optical equivalents $\varepsilon_{o/e}$, given by

$$\varepsilon_o = n_o^2 \qquad \varepsilon_e = n_e^2 \tag{7}$$

The dielectric permittivity tensor at optical frequencies then becomes

$$\varepsilon_{ij} = \varepsilon_o \delta_{ij} + \Delta\varepsilon n_i\, n_j \qquad (i,j = 1,2,3) \tag{8}$$

with $\Delta\varepsilon = \varepsilon_e - \varepsilon_o$. For the material dispersion of the LC, we use the Cauchy equation [15]

$$\begin{aligned} n_e(\lambda) &= A_e + \frac{B_e}{\lambda^2} + \frac{C_e}{\lambda^4} \\ n_o(\lambda) &= A_o + \frac{B_o}{\lambda^2} + \frac{C_o}{\lambda^4} \end{aligned} \tag{9}$$

with $\lambda$ the wavelength and $A_{e/o}, B_{e/o}, C_{e/o}$ the Cauchy coefficients for the extraordinary and ordinary refractive index, shown in Table 2. These have been obtained by measuring the refractive indices at visible wavelengths, and fitting Eq. 9 to the data. The refractive indices at infrared wavelengths are therefore an extrapolation of the refractive indices measured in the visible. For the wavelength dependence of the silica material we use the Sellmeier equation,

$$n^2(\lambda) = 1 + \sum_{i=1}^{3} \frac{B_i \lambda^2}{\lambda^2 - C_i} \tag{10}$$

with $B_i, C_i$ the Sellmeier coefficients for silica, shown in Table 2.

Table 2. The Cauchy coefficients for MDA-00-3969 and the Sellmeier coefficients for the silica material at room temperature

| $A_e$ | $B_e$ | $C_e$ | $A_o$ | $B_o$ | $C_o$ |
|---|---|---|---|---|---|
| 1.6681 | 0.01116 | 0.00192 | 1.47935 | 0.00513 | 0.00042 |

| $B_1$ | $B_2$ | $B_3$ | $C_1$ | $C_2$ | $C_3$ |
|---|---|---|---|---|---|
| 0.6961663 | 0.4079426 | 0.8974794 | 0.0684043 | 0.1162414 | 9.896161 |

The FEM simulations are set up a follows: First the geometry is constructed and the dielectric structure is assigned. The whole structure is then put on a grid, which has a small element size for the fiber core and the capillaries and a more coarse mesh elsewhere. The FEM system matrices are based on second order vector elements and the domain is truncated using Perfectly Matching Layer (PML) boundary conditions.

The FEM code is used to solve the generalized eigenvalue equation deriving from Maxwell's equations, and the core mode is obtained in wavelengths regions within a bandgap. We simulate the transmission spectrum for wavelength between 1200 and 1500*nm* by calculating the coupling loss, equivalent to the experimental situation where an LC infiltrated PCF is coupled to a PCF without LC. Mathematically, the coupling loss is given by the overlap integral of the core modes of both fibers, and taking both polarization directions into account, we obtain the

#105241 - $15.00 USD Received 12 Dec 2008; revised 31 Jan 2009; accepted 3 Mar 2009; published 5 Mar 2009

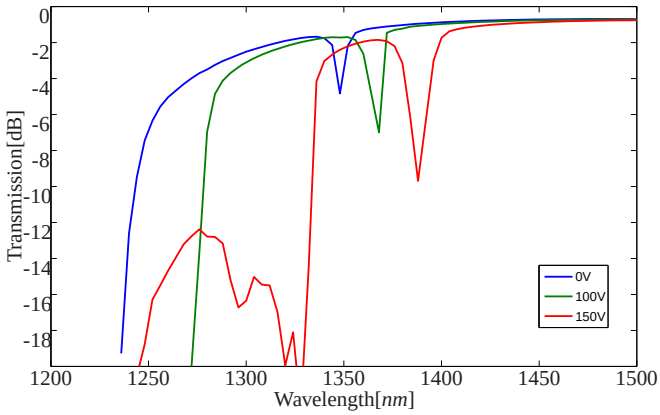


Fig. 9. The simulated transmission spectrum for an applied bias of 0V and 100V and 150V

relative transmitted power for the *i*- polarized $(i = 1,2)$ core mode as

$$p_i = \frac{\int\limits_{\Omega} d\Omega \left(|\mathbf{E}_i^{out} \cdot \mathbf{E_1^{inc}}|^2 + |\mathbf{E}_i^{out} \cdot \mathbf{E_2^{inc}}|^2\right)}{\int\limits_{\Omega} d\Omega |\mathbf{E}_i^{out}|^2 \left(\int\limits_{\Omega} d\Omega (|\mathbf{E_1^{inc}}|^2 + |\mathbf{E_2^{inc}}|^2)\right)} \tag{11}$$

with $\mathbf{E}_i^{out}$ the electric field of the *i*-polarized outgoing core mode and $\mathbf{E}_i^{inc}$ corresponding incoming one. In our case, we can neglect confinement losses, since we only infiltrate the fiber for 1cm length. Figure 9 shows the transmission spectrum for $0V$, $100V$ and $150V$ applied bias. The reorientation of the LCs due to an applied bias leads to a change of the mode structure in the capillaries, shifting the cutoff wavelengths. We obtain a bandgap shift of $36nm$ for $100V$

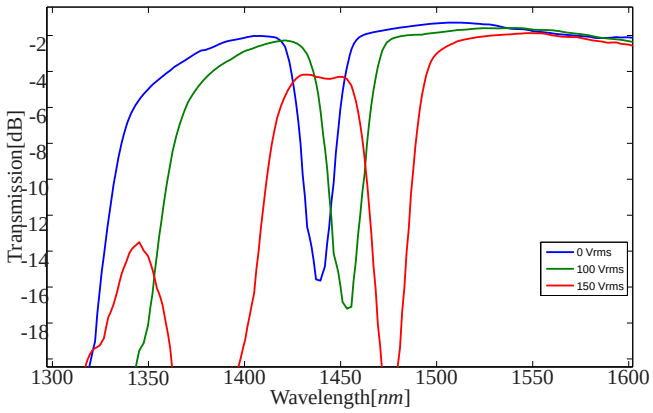


Fig. 10. The experimental transmission spectrum for 0Vrms, 100Vrms and 150Vrms potential difference

and $94nm$ for $150V$ at the short wavelength bandgap edge, while at the center of the notch we obtain a shift of $20nm$ and $42nm$ respectively. The short wavelength bandgap edge(-12dB) is at $1240nm$, $1276nm$ and $1334nm$ for the unbiased case, $100V$ and $150V$ respectively. The width of

#105241 - $15.00 USD Received 12 Dec 2008; revised 31 Jan 2009; accepted 3 Mar 2009; published 5 Mar 2009

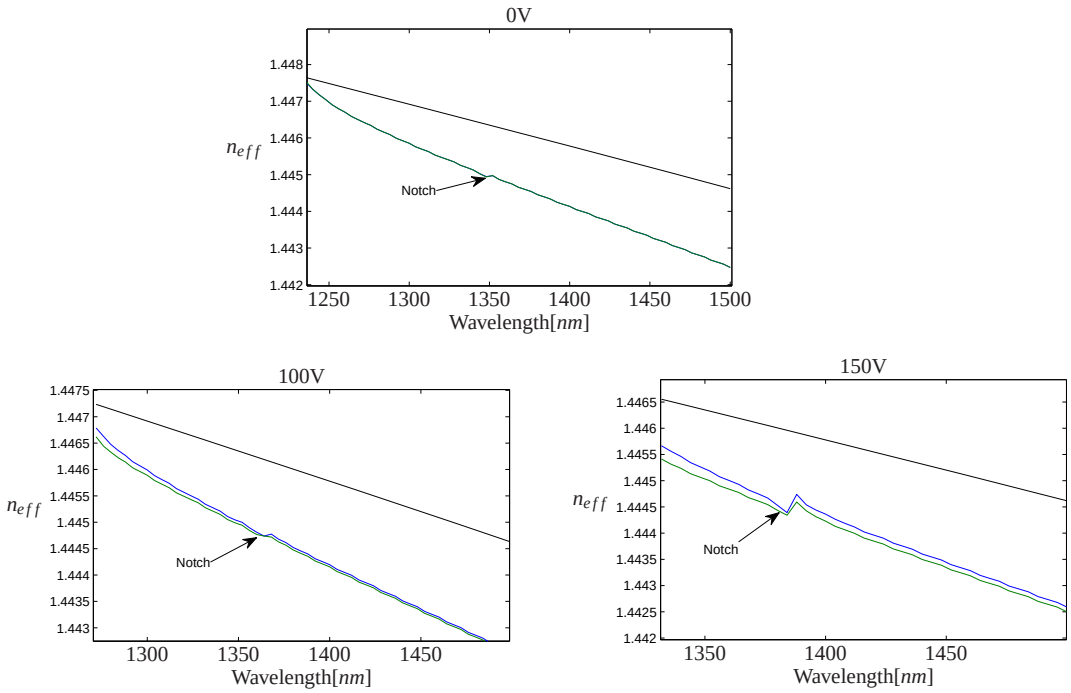


Fig. 11. The dispersion curves of the bandgap guided modes for 0V, 100V and 150V. The black line shows the dispersion curve for silica

the bandgap, measured from the short wavelength edge to the center of the notch is 108$nm$ in the unbiased case, 92$nm$ for 100$V$ bias and 56$nm$ for 150$V$. We compare these values with the ones obtained in the experiment. The experimental spectrum is shown in Fig. 10. The bandgap shift is 28$nm$ for 100$V$ and 80$nm$ for 150$V$ at the short wavelength edge and 15$nm$ and 38$nm$ respectively at the notch. The short wavelength bandgap edge is at 1330$nm$ in the unbiased case and 1358$nm$ and 1410$nm$ for 100$V$ and 150$V$ respectively. The width of the bandgap from the short wavelength edge to the center of the notch is 108$nm$, 95$nm$ and 66$nm$ for 0$V$, 100$V$and 150$V$ applied bias respectively. The width and the depth of the notch in the experimental spectrum are significantly greater then the ones in the simulated spectrum. This is due to a slightly varying hole size for the experimental fiber, supporting more modes in the capillaries and resulting in a wider wavelength range for which the core mode couples to the cladding modes. Nevertheless, the simulated bandgap shift, the bandgap width and shape are in very good agreement with the experimental ones.

Figure 11 shows the dispersion curves of the bandgap guided modes for the three voltages as well as the material dispersion of silica. The position of the notch is at the discontinuity of the disperion curves. For 0$V$ applied bias, the two polarization directions of the core mode have identical effective indices at all wavelengths, due to the symmetry of the structure. For 100$V$ and 150$V$ applied bias the polarization directions split up, since the reorientation of the director brakes this symmetry. One polarization direction 'sees' a higher average refractive index than the other, leading to a higher effective index. For 100V, this splitup is between $\Delta n_{eff}(1.5\mu m) = 3.5\times10^{-5}$ and $\Delta n_{eff}(1.272\mu m) = 1.85\times10^{-4}$ while for 150V it ranges from $\Delta n_{eff}(1.5\mu m) = 9\times10^{-5}$ to $\Delta n_{eff}(1.332\mu m) = 2.53\times10^{-4}$.

The whole simulated spectrum is shifted about 100$nm$ with respect to the experimental case. Reasons for this are, that the average capillary size of the experimental fiber varies slightly from

#105241 - $15.00 USD Received 12 Dec 2008; revised 31 Jan 2009; accepted 3 Mar 2009; published 5 Mar 2009

the one we use in the simulations which is taken from the datasheet for the LMA-13 fiber, and that the refractive indices are extrapolations from the values in the visible. Both, the value of the refractive indices and the hole radius are critical for the position of the bandgap. The influence of both contributions can be estimated with the ARROW-formula [16],

$$\lambda_m = \frac{2d}{m+1/2}\sqrt{n_2^2 - n_1^2} \tag{12}$$

where $\lambda_m$ is the $m$-th order transmission-minimum wavelength in the spectrum, $d$ the hole diameter and $n_2$ and $n_1$ the (average) refractive indices of the LC and silica respectively. A small deviation in hole diameter or refractive index therefore leads to a change of the bandgap position.

## 4. Conclusion

We simulate, for the first time, the alignment of LCs with an applied external bias for all capillaries of a PCF. We use an iterative approach to solve the system of coupled PDEs, namely Poisson's equation and the minimization of the free energy, and obtain the spatially varying dielectric tensor structure. We obtain the transmission spectrum and the bandgap shift for $100V$ and $150V$ applied external bias. We find a shift of $36nm$ and $94nm$ at the short wavelength edge and $20nm$ and $42nm$ at the notch, for $100V$ and $150V$ respectively. In the corresponding experimental spectrum the bandgap shift is $28nm$ for $100V$ and $80nm$ for $150V$ at the short wavelength edge and $15nm$ and $38nm$ respectively at the notch. The shape of the transmission spectrum as well as the bandgap shift are in good agreement with the experimental ones. Our simulation scheme can be used to simulate arbitrary LCPCF combinations. Furthermore, it can easily be expanded for simulating the cladding mode structure to obtain a better understanding of the mechanisms of the bandgap shift and split-up of the cladding modes, which opens up the possibility to characterize LCs and PCFs according to their parameters. In this way we will be able to systematically investigate LCPCF combinations suitable for optical devices.

#105241 - $15.00 USD Received 12 Dec 2008; revised 31 Jan 2009; accepted 3 Mar 2009; published 5 Mar 2009